Research Article | Vol. 9, No. 5 / 1 May 2019 / Optical Materials Express 2006

Optical Materials EXPRESS

Tunable green lasing from circular grating distributed feedback based on $CH_3NH_3PbBr_3$ perovskite

MATTHÄUS JÄCKLE,[1,*] HEIKO LINNENBANK,[1] MARIO HENTSCHEL,[1] MICHAEL SALIBA,[2] SERGEI G. TIKHODEEV,[1,3] AND HARALD GIESSEN[1]

[1]4th Physics Institute and Research Center SCoPE, University of Stuttgart, Pfaffenwaldring 57, Stuttgart 70569, Germany
[2]Adolph Merkle Institute, University of Fribourg, Chemin des Verdiers 4, 1700 Fribourg, Switzerland
[3]Laboratory of Photomolecular Science, Lomonosov Moscow State University, Moscow, 119991, Russia
[*]m.jaeckle@pi4.uni-stuttgart.de

Abstract: We demonstrate tunable green lasing from a bromide-based organic-inorganic perovskite thin-film. The optical feedback required for laser emission is provided by a circular grating that forms a disk Bragg resonator inside a spin-coated 200 nm thin-film of methylammonium lead tri-bromide ($CH_3NH_3PbBr_3$). As the emission spectrum below as well as above the lasing threshold is reasonably affected by the Bragg grating resonance, it becomes possible to engineer and thus tune the emission between 541 and 552 nm. Our study incorporates the influence of the temperature on both the linear optical properties as well as the emission.

1. Introduction

Organic-inorganic metal-halide perovskites are semiconductors with exceptional material properties which enable them as a future optical material for photovoltaics and light generation. They have a direct bandgap [1] with a strong absorption in the near-infrared and visible wavelength region [2] and a high charge carrier mobility [3]. Additionally, to these optical material properties they are solution processable and their bandgap can be tuned over the entire visible spectrum by varying the halide composition [4], where the bandgap for I based materials is at 1.5 eV, for Br based materials at 2.3 eV and for Cl based materials at 3.1 eV [5,6]. The research in the last years was focused on the development of perovskite solar cells based on $CH_3NH_3PbI_3$ due to its high absorption in the entire visible spectral range. The conversion efficiency was increased from 3.8% [7] in 2009 to 23.7% in 2019 [8]. The combination of exceptional electro-optical properties, low material costs and possible facile fabrication, make perovskites also very attractive for light generation devices such as LEDs or lasers. In recent years perovskite LEDs have shown an increase in external quantum efficiency for red, green, blue and white light emission [9–12]. In order to generate coherent light from perovskites, several different optical feedback mechanism and structures have been studied. For example, the first realized perovskite laser used a Fabry–Pérot cavity [13], other confirmed devices utilize nanowire structures [14], whispering gallery mode resonators [15,16] as well as simple 1-D distributed feedback (DFB) structures for iodide [17–19], bromide [20,21] and all-inorganic [22] based perovskites. Apart from the material composition these different realizations of perovskite DFB lasers employ different fabrication processes and report on stimulated emission under the excitation of different pump regimes. The most common fabrication process was nanoimprint lithography of a normal DFB structure on perovskite thin-films synthesized by evaporation, spin-coating, nanocrystal-pinning or inkjet printing, which produces films with nm roughness. All of the mentioned results for achieving stimulated emission were measured under ns excitation pulses at repetition rates in

#357534 https://doi.org/10.1364/OME.9.002006
Journal © 2019 Received 14 Jan 2019; revised 15 Mar 2019; accepted 16 Mar 2019; published 2 Apr 2019

Optical Materials EXPRESS

the kHz range but for I based perovskites also stimulated emission under continuous wave (cw) excitation was reported [18]. The thresholds at room temperature ranged from 0.32 up to 6 μJ cm^{-2} for the organic-inorganic methal-halide perovskites, 54 μJ cm^{-2} for the inkjet printed perovskite and 33 μJ cm^{-2} for the all-inorganic perovskite. Based on these approaches, the final goal would be to combine these feedback mechanisms with the entirely solution processable material resulting in electrically driven LEDs [23] or an electrically pumped, easy to fabricate, cw laser operating at room temperature.

Here, we investigate the realization of a solution-processed circular DFB structure made of methylammonium lead tri-bromide ($CH_3NH_3PbBr_3$). Circular Bragg gratings with varying grating periods on a glass substrate are covered with a thin perovskite film deposited by spin-coating. Also, these films are neither flat, in the sense that the grating as a whole is covered by a perovskite layer, nor smooth compared to the operation wavelength. Nevertheless, we can clearly resolve waveguiding and resonant optical feedback by optical extinction measurements. Evaluating both, the linear properties of the DFB structures as well as the optical emission over a wide temperature range we observe stimulated emission matching the individual grating resonances. The observed emission covers the entire luminescence emission band of methylammonium lead tri-bromide from 541 to 552 nm at temperatures up to 240 K. The achieved laser wavelength region around 550 nm is one of the crucial three wavelengths for the efficient generation of colors in laser projectors, which shows a larger possible color range than LED based projectors [24]. One of the problems for the realization of such lasers is the so called green-gap at exactly this wavelength in the emission efficiency of InGaN and AlGaInP based diodes [25].

2. Circular DFB grating

A distributed feedback cavity is a well-known realization of a laser resonator, which is generated by the wavelength-selective constructive interference of reflections at the interfaces of a periodic refractive index grating incorporated into a waveguide [26]. By fabricating the gain medium as a waveguide, as can be achieved with thin-films, a monolithic laser design without any external cavity can be realized. Additionally, such a μm-sized laser can be directly integrated into opto-electronical circuits [27,28]. The simplest realization is a 1-D grating employing 2nd order Bragg Reflection for surface emission perpendicular to the grating [29,30]. In a first approximation the resonance wavelength of a 2nd order Bragg grating has to fulfill the following condition:

$$\lambda_{Bragg} = \frac{2\Lambda n_{eff}}{m} \tag{1}$$

with resonance wavelength λ_{Bragg}, order $m = 2$, grating period Λ, and effective refractive index n_{eff} composed of the material refractive index and waveguide geometry.

For our studies we use a more advanced 2-D grating. The structure consists of a substrate which is covered with an approximately 200 nm thick thin-film of $CH_3NH_3PbBr_3$, where the film acts as waveguide. The DFB structure itself, which is etched into the glass substrate, is composed of an unstructured central disk surrounded by a concentric, periodic circular grating. The resonating light is thus vertically confined in the gain medium and horizontally concentrated in the central disk. The grating provides both the optical feedback and couples the emission out of the perovskite thin-film. The advantages of this structure are a low possible threshold by concentrating the light in the central disk [31], a circular symmetric far-field beam with a narrow divergence, and a good emission efficiency because most of the outcoupled light is emitted in the zero-order mode [32]. A disadvantage is the high possibility of multi-mode emission caused by the low threshold and the small mode discrimination of such a grating structure [31].

The circular gratings are fabricated in several steps. First, standard electron beam lithography in poly(methyl methacrylate), electron gun evaporation, and subsequent lift-off is used to prepare a chromium etch mask. This mask is then transferred into the glass substrate by reactive plasma

Optical Materials EXPRESS

etching (ECR-RIE) with Freon (CHF_3). The remaining chromium is removed with a commercial liquid etching solution. The result is displayed in the SEM images in Fig. 1(a) which depicts a section of the unstructured central disk with a diameter of 20 µm and the surrounding grating with 100 µm diameter. Figure 1(b) shows the structure after a FIB cut, which reveals a modulation depth of 80 nm, a groove width of 150 nm, and an elevation width of 130 nm. Several different structures with grating periodicities between 261 and 286 nm were produced on the same substrate. The periodicities are chosen according to Eq. (1) and an estimated effective refractive index of the perovskite thin-film of approximately 2.0, derived from a material refractive index of 2.29 [33], to realize grating resonances at wavelengths slightly above the bandgap of 539 nm.

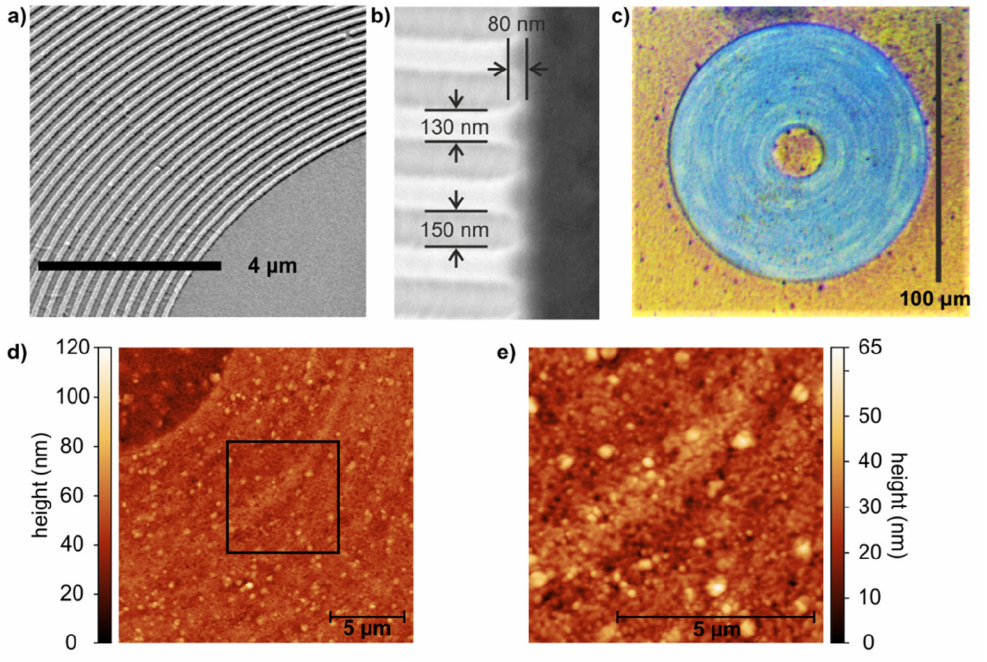

Fig. 1. (a) SEM image showing the circular grating surrounding the flat central disc. (b) FIB cut of the grating visualizing its dimensions. (c) Microscope image of a circular DFB structure spin-coated with $CH_3NH_3PbBr_3$. (d) AFM image of a spin-coated grating surrounding the central disk, whereas the marked square is enlarged in figure (e).

The perovskite solution which is synthesized by blending MABr (1.2 M) and $PbBr_2$ (1.2 M) in an anhydrous dimethylformamide (DMF:DMSO) solution with a ratio of 4:1. The perovskite was spin-coated onto the glass substrate with the circular grating in a two-step process at 1000 and 6000 rpm for 10 and 30 s respectively. During the second step, 100 µl of chlorobenzene was poured on the spinning substrate 15 s before the end of the procedure. Afterwards, the sample was annealed at 100 °C for 1 h in a nitrogen atmosphere glove box [34,35]. The resulting thin-film has a thickness of 200 nm. In Fig. 1(c) an optical microscope image of the final structure is shown. It seems to reveal that the thin-film is not homogeneous above the structure, especially with respect to the difference between the flat central disc and the surrounding grating. However, from the AFM image in Fig. 1(d) it becomes evident that the average height difference only amounts to 15 nm. The circular corrugation which is apparent both in the optical and the AFM image is the same order but has a periodicity of several µm and is thus much larger than the actual grating (see. Figure 1(a)). Figure 1(e) depicts a zoom-in of Fig. 1(d), which reveals a rms-roughness of 6.4 nm, which is comparable to reported thin-film perovskite DFB lasers. But there are several grains visible with heights of up to 40 nm and diameters of several hundred nm, being on the

Optical Materials EXPRESS

same order as the grating geometry. These deviations from a perfectly flat and homogeneous thin-film reduce the performance of the samples. However, no post-treatments were used in this proof-of-concept study outlining first strategies for process optimization in future works.

3. Stimulated emission

In the following the circular structures are investigated with respect to their ability for lasing operation under pulsed optical pumping. The grating resonances responsible for the optical feedback are characterized by white-light transmission spectroscopy. For this a fiber coupled thermal light source is focused to a spot diameter of 90 µm on the sample. A 200 µm pin-hole in front of the focusing lens is used to reduce the angular distribution of the white light. The transmitted light is dispersed with a SpectraPro 500i grating monochromator (Acton) with a grating density of 1800 mm^{-1} and analyzed with a Pylon 400 F liquid nitrogen cooled Si-CCD-Camera (Roper Scientific). The grating resonances are acquired relative to the transmission through a bare perovskite thin-film. Optical pumping at a wavelength shorter than 539 nm is required to achieve population inversion. For this a PolarOnyx Yb fiber laser with 1030 nm wavelength, pulse duration of 400 fs, and a repetition rate of 37 MHz is frequency doubled with a thin LBO crystal to generate sub-picosecond pulses. In order to reduce the thermal load on the perovskite, a chopper wheel running at 100 Hz with ≈3000 pulses per opening is used. Each pump sequence has thus a length of 80 µs which together with the high repetition rate mimics the thermal load which would occur during cw pumping. The pump beam is then focused through the glass substrate onto the perovskite to a diameter of 80 µm. The excited emission is collimated by a lens with an NA of 0.4 and analyzed by the same system as mentioned above, whereas a tilted 550 nm long pass filter is used to block the residual pump light. The sample is mounted inside a liquid helium-cooled MicrostatHe2 cold-finger cryostat (Oxford Instruments) with a temperature accuracy of 0.2 K. The sample was kept under vacuum conditions to prevent chemical degradation through humidity [36].

Figure 2 displays the results upon optically exciting the perovskite thin-film. For these measurements the structure with a period of 271 nm was excited at 5 K. The red curve in Fig. 2(a) and (b) indicated by the red squares in 2(c) and 2(d) are recorded at a pump energy density of 1.9 µJ cm^{-2}. Here, only a dip in the spectrum of the photoluminescence is visible at 546 nm, originating from the grating resonance which is indicated by the black curve in Fig. 2(a). By increasing the pump density from 1.9 to 2.4 µJ cm^{-2}, a sharp emission peak emerges at this spectral position, as visible in the green curve in Fig. 2(a) and (b). As depicted in Fig. 2(d) this emission peak has a linewidth of only 0.6 nm, compared to the 9 nm of the photoluminescence emission. Increasing the pump density further to 3 µJ cm^{-2} leads to a very strong increase of the emission intensity as visible in Fig. 2(b) and (c). The emission peak experiences spectral broadening as well as a shift to shorter wavelengths due to the increasing density of excited carriers and excitons, which lead to a band filling, a shift of the quasi-Fermi levels and to exciton screening [37,38]. In addition, the stronger pumping will lead to a local heating, whereby a blue-shift can occur in $CH_3NH_3PbBr_3$ [39]. By further increasing the pump density to 10.8 µJ cm^{-2} a saturation of the emission efficiency can be clearly seen in Fig. 2(c). Likewise, a saturation of the broadening can be observed in the values of the extracted FWHM shown in Fig. 2(d). Simultaneously, a second emission peak occurs at a slightly longer wavelength as visualized in Fig. 2(b). This second peak at 550 nm contains the amplified spontaneous emission (ASE) and was also observed from the photoluminescence emission from bare perovskite, which can be seen in the appendix Fig. 12. In contrast to the blue-shift of the narrow emission peak, the second peak experiences a red-shift for increasing pump energy, as expected for ASE [40,41]. These observations, the threshold behavior, the saturation, as well as the linewidth narrowing are characteristic for lasing operation. Analogous measurements with consistent results are

Optical Materials EXPRESS

performed for several grating periods and temperatures as provided in Figs. 8–11 in the appendix data.

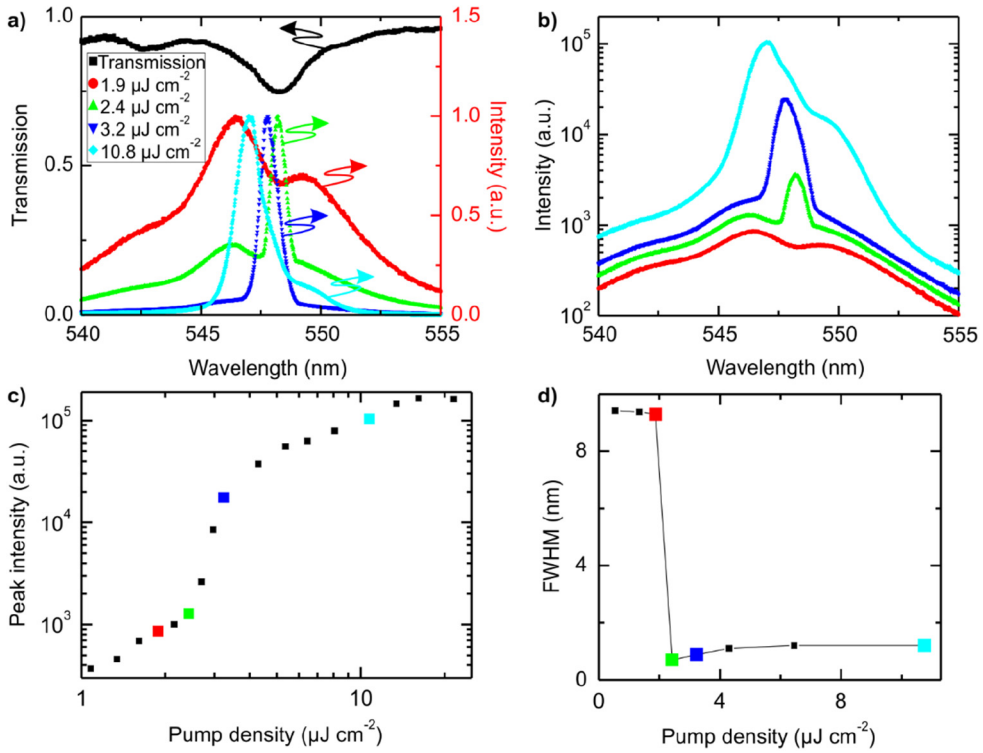

Fig. 2. (a) (colored, right axis) Emission spectra for different pump densities normalized to their individual maximal value along with the linear transmission spectrum (black, left axis) of the DFB grating. b) Same spectra as in (a) plotted in a logarithmic scale. (c) Peak intensity of the emission as function of the pump density for a grating period of 271 nm at 5 K. (d) FWHM of the emission plotted as a function of the pump density.

A further characteristic of laser emission is a strong degree of polarization compared to unstimulated photoluminescence. In Fig. 3 three polarization dependent measurements are presented, one for the photoluminescence from an unstructured part of the sample, the second from the structure with 271 nm grating period and a pump power below threshold, and from the same structure with a pump power significantly above threshold. For these measurements a rotatable linear polarization filter was inserted in front of the spectrometer.

In Fig. 3(a) the normalized peak intensities are visualized as a function of the polarizer angle, whereas in Fig. 3(b) the spectra without a polarization filter are plotted. The photoluminescence from the unstructured area shows an undefined polarization state. In contrast, the emission from the structured area below threshold shows a difference between a polarization angle of 45° and 135° introduced by the grating itself. From symmetry considerations one would not expect any preferential polarization direction from a circular grating. However, in a real world experiment the emission from the perovskite film will not be uniformly distributed across the grating but will show some spatial gradient due to a non-central or tilted illumination, thus the diffraction for a certain polarization will be preferred. As soon as the stimulated emission above threshold sets in, the emitted light will hence show a strong polarization in this preferred direction, as can be seen in the near zero emission under a polarization filter angle of 120° for the lasing spectra.

Optical Materials EXPRESS

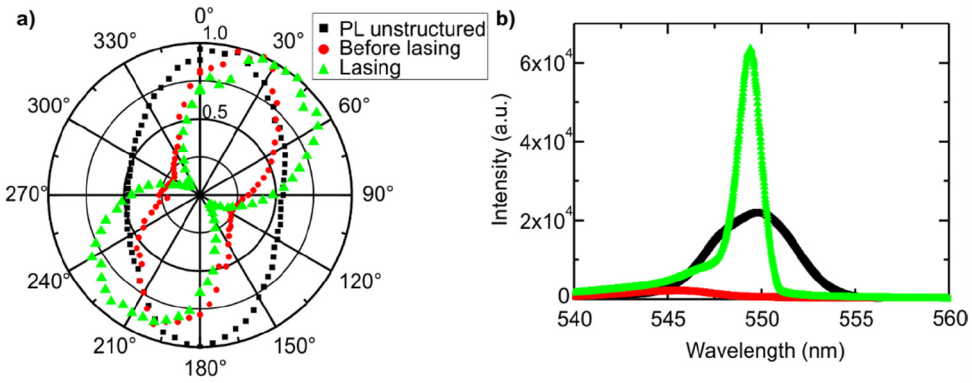

Fig. 3. (a) Normalized peak intensity plotted for different polarization angles to compare the emission from photoluminescence (black), structure with a pump power below threshold (red) and above threshold (red). (b) Measured spectra without a polarization filter.

4. Tunability

From Fig. 2(a) it becomes evident that the wavelength of the laser emission is determined by the resonance of the grating. In a first approximation the grating resonance follows the condition for second-order Bragg diffraction in 1 D gratings given by Eq. (1).

Figure 4(a) shows the linear transmission spectra for different grating periods ranging from 261 to 286 nm at a sample temperature of 5 K. The resonance wavelength changes from 546 to 553 nm. Intuitively one would expect with respect to Eq. (1) a broader tuning range due to the variation of the investigated grating periodicities. However, the effective refractive index is constituted by both the material and the waveguide and thus a strong wavelength dependence is expected. Additionally, the difference between 1-D gratings and circular gratings is neglected here. The resulting emission spectra above threshold are plotted in Fig. 4(b). The structure with a periodicity of 286 nm shows no lasing emission. The wavelength of the lasing emission peak increases with increasing grating periodicity although there is no exact match.

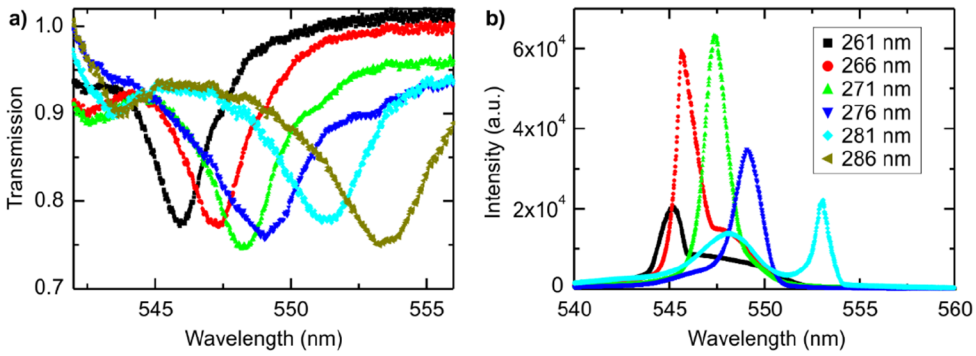

Fig. 4. (a) The transmission spectra of different grating periods at 5 K normalized to an unstructured part of the perovskite thin-film. (b) Laser emission from the different gratings at 5 K at a pump density of 6.5 μJ cm^{-2}.

In general lasing emission occurs at the overlap between the resonance of the optical cavity and the intrinsic gain of the active medium. The latter can be characterized by the photoluminescence spectrum. From Fig. 2d the spectral width of the photoluminescence is approximately 9 nm

Optical Materials EXPRESS

which corresponds to the emission from 545 to 553 nm. All spectra in Fig. 4(b) are excited with the same pump density, thus the intrinsic gain of the perovskite is given by the photoluminescence which is resembled in the yield of the laser emission. Obviously, the overlap between the grating resonance of the structure with the periodicity of 286 nm and the intrinsic gain is too weak to support laser emission.

By comparing the exact wavelengths in Fig. 4(a) and 4(b) a small deviation between the resonance position and its corresponding emission can be found. The white light transmission measurement is only suited for measuring the far-field scattering and not the local intensity distribution inside the gain medium which influences the laser emission wavelength.

Additionally, the influence of the inhomogeneity of the spin-coated perovskite thin-film, which was mentioned before, influences both the spectral position of the transmission and emission measurements. Visible spectral shifts of ± 1 nm are observed by small changes of the excitation position.

By adapting the grating period and thus the resonance one can engineer a laser with a wavelength which is suited best for the desired application, only restricted by the spectral width of the photoluminescence.

5. Temperature dependence

In Fig. 5(a) the central wavelength of the grating resonance is plotted over a temperature range from 5 K to 240 K for gratings with periodicities from 261 to 281 nm. The wavelength was obtained by fitting a Gaussian peak to the measured transmission spectra. By increasing the temperature, the grating resonance exhibits a linear blue-shift of approximately 7 nm over a temperature difference of 235 K for all gratings. This shift is induced by the influence of the temperature dependent refractive index of the perovskite on the grating resonances. Regarding the resonance condition for second-order Bragg grating given by Eq. (1) the results from Fig. 5(a) indicate a decrease of the effective refractive index for increasing temperatures. It is well known that the bandgap of $CH_3NH_3PbBr_3$ exhibits a blue-shift with increasing temperature [39,42] which results in a decrease of the refractive index for wavelengths longer than the bandgap energy [33]. Figure 5(b) shows the wavelength of the laser emissions relating to the gratings from Fig. 5(a) over the same temperature range. This wavelength was also obtained by fitting a Gaussian peak to the measured spectra. The pump density for all emission spectra was slightly above their individual threshold to reduce the influence of the pump density dependent blue-shift on the comparability of the wavelengths. As expected from the behavior of the grating resonances,

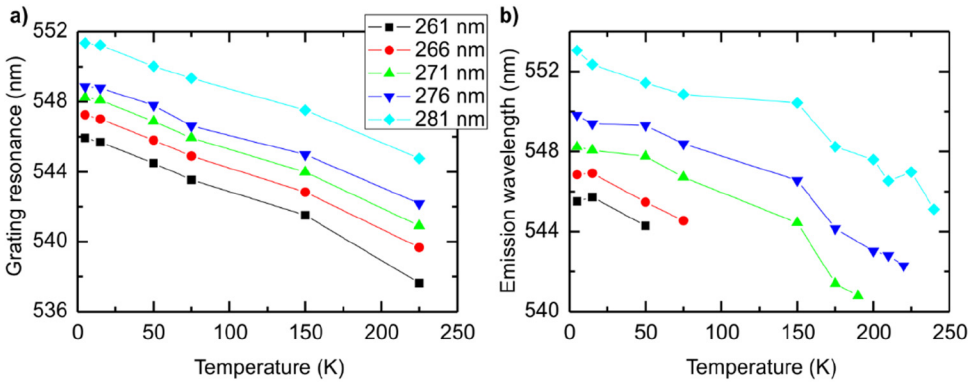

Fig. 5. (a) Center wavelength of the grating resonance as a function of temperature for the different grating periods. (b) Wavelength of the laser emission over temperature for different periods.

Optical Materials EXPRESS

the emission wavelengths also blue-shifts linearly for increasing temperature. The deviation between the exact central wavelength of a resonance at a certain temperature and its emission wavelength was discussed previously. The structures with a small grating period of 261 and 266 nm and thus the structures with the shortest emission wavelength have a low maximal temperature between 50 and 75 K respectively for supporting laser emission. The structures with greater periodicities have maximal emission temperatures higher than 175 K and the structure with a grating period of 281 nm exhibits laser emission even at 240 K.

In Fig. 6 in the appendix the emission from the structure with a grating period of 281 nm is plotted exemplary. The general spectral shape of the laser emission remains constant. The laser emission is slightly red-shifted with respect to the photoluminescence maximum but both experience the same blue-shift with increasing temperature. Yet a strong decrease of the yield with increasing sample temperature is apparent. This can also be retrieved from a study of the temperature dependency of the threshold which is presented in Fig. 7. Here an exponential increase with increasing temperature is observed.

The structure with the grating period of 281 nm was not the most efficient at 5 K due to the fact that its resonance was not coincident with the maximum of the photoluminescence as visible in Fig. 4(b). Nevertheless, it is the only structure which shows laser emission close to room temperature. This is most likely due to the fact that it is further away from the absorption edge of the bandgap as the other grating resonances. Thus it will experience less additional absorption from the broadening of the Urbach tail with increasing temperature [43]. This influence of the absorption at the short wavelength edge of the photoluminescence can be obtained from appendix Fig. 8(a) where the structure with a periodicity of 261 nm shows the lowest emission intensity comparing to the other structures at this temperature. Although both, the bandgap and the resonance wavelength are blue-shifting with increasing temperature this might not be at the same rate. Figure 5(b) supports this suggestion, as no emission has been obtained from the structures with a periodicity of 261 nm and 266 nm at temperatures above 50/75 K. The favored amplified emission at longer wavelengths due to the lower absorption is likewise visible by the occurrence of ASE in this spectral region, as can be seen in the appendix Fig. 12.

The threshold pulse energy density at 240 K was 21 μJ cm^{-2} which is higher than the thresholds reported in previous publications about Br based DFB perovskite lasers at room temperature [20,21], although the circular grating should have a lower threshold than the normal DFB design. This discrepancy can be explained by the thin-film quality as well as the different pump regime. With a MHz repetition rate excitation laser, in contrast to the previous used kHz lasers with higher light fluence, the thermal load deposited on the sample is comparable to cw excitation. In contrast to other studies, no post-treatment of the used thin-films has been employed in order to reduce the roughness and waviness. The resulting scattering will most likely limit the waveguiding properties of the films. Thus, a comparable threshold is noteworthy.

6. Summary

In summary we demonstrated stimulated true-green laser emission from $CH_3NH_3PbBr_3$ spin-coated circular DFB structures from 541 to 553 nm, excited by high repetition rate pulsed optical pumping. The emission exhibits a typical threshold and saturation behavior, with thresholds as low as 2.5 μJ cm^{-2} and a spectral FWHM of 0.4 nm. Additionally, it shows a significant polarization dependence for pump densities above threshold. The wavelength of the laser emission is determined by the grating resonance, which can be tuned over a range of approximately 9 nm by varying the grating periodicity from 261 to 281 nm. For increasing temperatures, the grating resonance and thus the laser emission exhibits a linear blue shift and not a red shift in accordance with the unusual temperature dependence of the bandgap known for organic-inorganic perovskites. This leads to a decrease in the possible wavelength tuning range of the fabricated structures caused by an increased absorption for short wavelengths through broadening of the Urbach-tail.

Optical Materials EXPRESS

Nevertheless, laser emission was observable for sample temperatures up to 240 K. Based on the presented structures prospective geometries with resonances both further away from the absorption edge and closer to the true green 550 nm emission could be designed. Future work will focus on an improved geometry by tailoring the circular grating all the way to the center and thus varying the central disk diameter, as well as tailoring the remaining waveguide properties, especially the thin-film quality, to design gratings which support lasing thresholds low enough to enable room temperature lasing.

A. Appendix

A.1. Emission from 281 nm grating period for temperatures from 5 to 240 K

In Fig. 6(a) the spectra of the 281 nm grating period structure are plotted for different temperatures. The pump density was slightly above the threshold. In order to better compare the spectral shape of the emissions the spectra from Fig. 6(a) were normalized to their individual maximum value and plotted in Fig. 6(b).

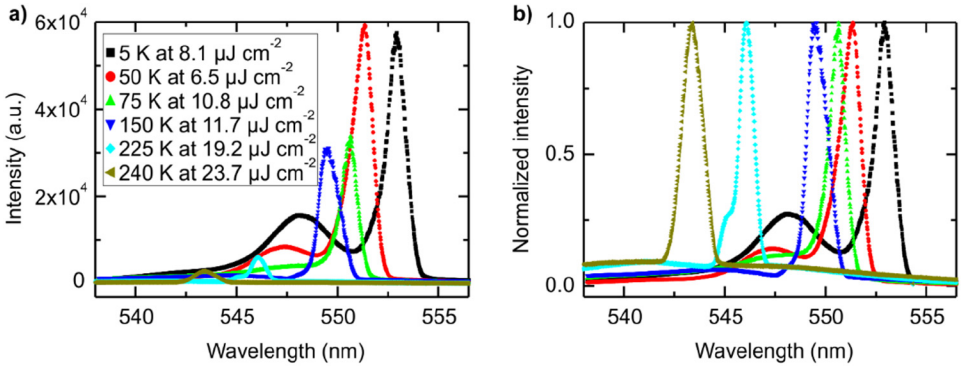

Fig. 6. (a) Emission spectra for 281 nm grating period at different temperatures close to the threshold pump density. (b) The same spectra normalized to each maximal value.

The emission from this structure blue-shifts from 553 nm to 545 nm for increasing temperature, due to a blue-shift in the grating resonance. The threshold increases also for increasing temperatures except between 5 K and 50 K. This can be understood as follows. At 5 K the resonance is at the edge of the photoluminescence, thus the intrinsic gain is weak. For 50 K the photoluminescence yield and thus the gain should decrease, but the resonance blue-shifts closer the maximum of the intrinsic gain. The smallest threshold energy density is 6.5 μJ cm^{-2} and the highest is 23.7 μJ cm^{-2}. The same behavior can be seen for the yield of the emission which decreases for increasing temperature except between 5 K and 50 K because of the same reason as the threshold. From Fig. 6(b) it becomes evident that the spectral width as well as the overall shape does not change significantly with increasing temperature.

A.2. Lasing threshold versus temperature behavior

In the Fig. 7 the thresholds of all structures are plotted as function of the temperature. The thresholds were obtained by linearly fitting the slope of the peak intensity of the photoluminescence, as well as the increased slope of the peak intensity after the threshold.

The threshold increases exponentially over temperature from 2.5 μJ cm^{-2} at 5 K to 22 μJ cm^{-2} at 240 K.

Optical Materials EXPRESS

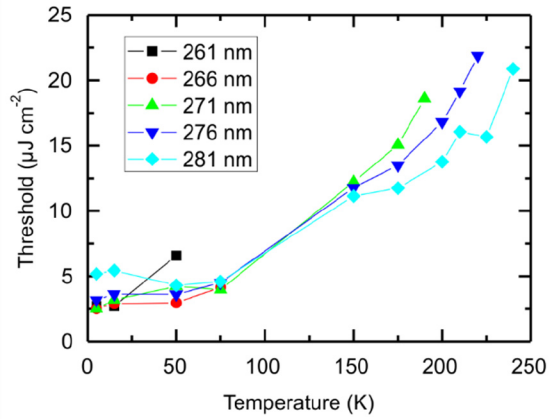

Fig. 7. Threshold density as a function of temperature for different grating periods.

In this plot it can also be seen that structures with shorter grating period stop lasing at certain temperatures, as well as an increasing threshold before this temperature. This can be clearly seen for 261 nm at 50 K, 271 nm at 190 K and 276 nm at 220 K.

A.3. Linear and logarithmic spectra

The following Figs. 8–11 show an overview of the emission spectra for several grating periods at temperatures of 5 K, 75 K, 150 K and 225 K on a linear and a logarithmic scale. The periods at each temperature except 225 K were chosen to represent the short wavelength range, the maximum and the long wavelength range of the photoluminescence. At 225 K there is only one structure left, showing stimulated emission. Also, the power levels were chosen to be just before threshold (black), right after the threshold (red), at lasing operation (green), and after the saturation (black).

The two different plots have the advantage of emphasizing different properties of the spectra. In the linear plots the peak intensities and the spectral widths of the emissions with a large excitation density can be clearly compared, while the logarithmic plots are more suited to visualize the behavior at low excitation densities as well as the shape of the residual unstimulated emission.

The general behavior of the spectra for increasing pump energy density remains the same for all temperatures and grating periods. There is a visible dip in the photoluminescence below threshold which results from the resonance of the circular DFB grating. Above threshold there is a narrow peak emerging from the resonance dip. For an increasing pump density, the peak intensity is strongly growing and blue shifts. The growth of the intensity slows down after reaching the saturation pump energy and can even reverse.

The 261 nm structure has a low lasing threshold and exhibits a narrow emission but the position of its emission is in the short wavelength part of the photoluminescence and by blue-shifting over temperature the intrinsic gain becomes weaker. This leads to an early saturation where an increase of the pump energy doesn't increase the peak power anymore.

The structure with a resonance located nearby to the PL maximum but also on the longer wavelength side has a periodicity of 271 nm. This shows a low threshold but also a significant higher saturation point in comparison to the 261 nm structure. Here, the reduction of peak growth is smaller. In the logarithmic spectra another peak at 550 nm which comes from amplified spontaneous emission from the photoluminescence is visible. This peak was also observed for unstructured parts. It has a higher threshold than the lasing emission and red-shifts for increasing temperature.

Optical Materials EXPRESS

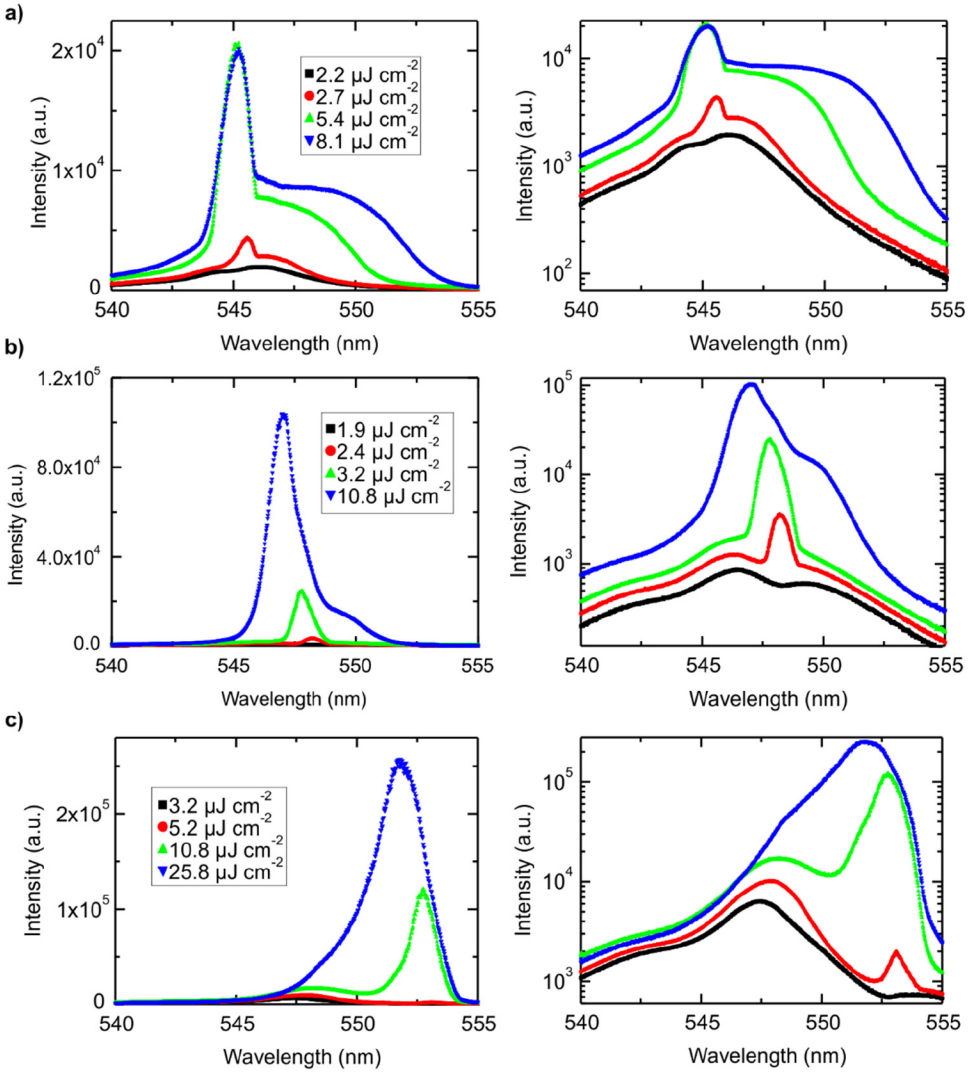

Fig. 8. Linear and logarithmic spectra for (a) 261 nm, (b) 271 nm and (c) 281 nm grating period at 5 K at different excitation densities.

Optical Materials EXPRESS

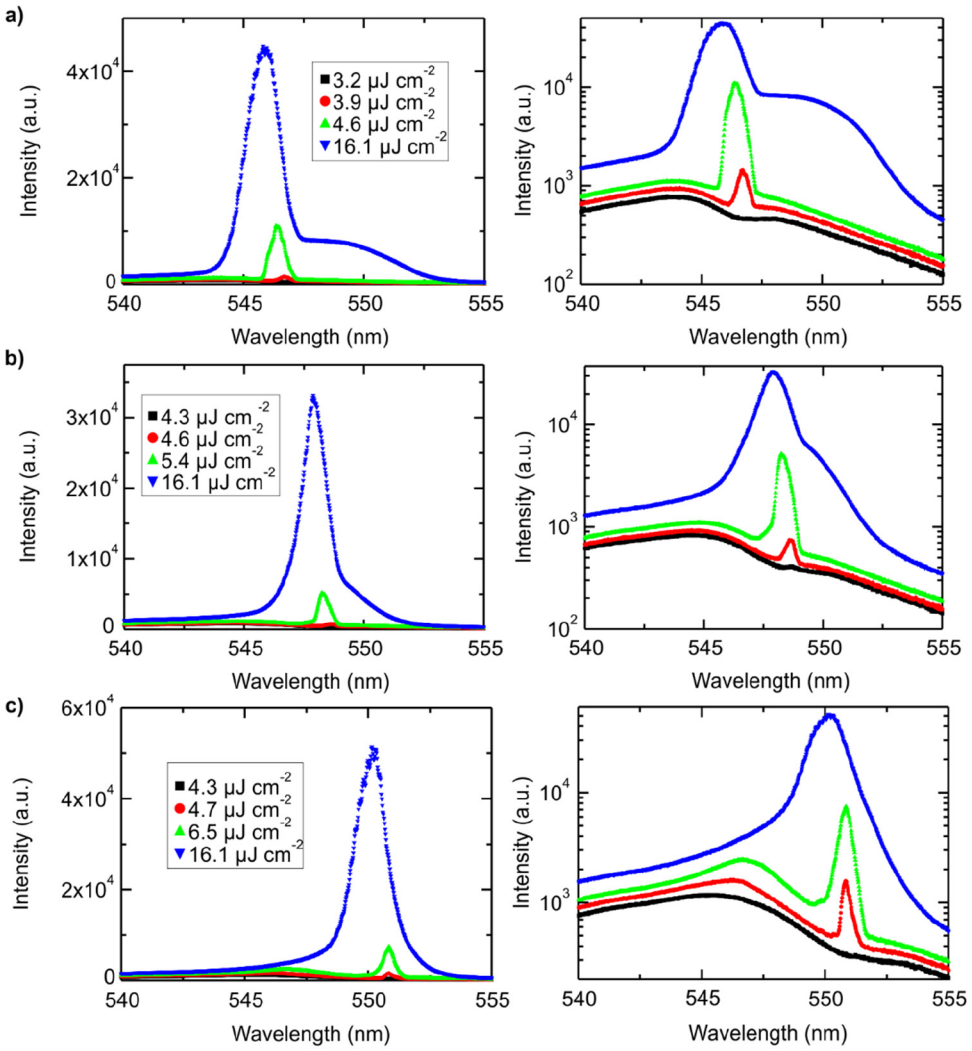

Fig. 9. Linear and logarithmic spectra for (a) 271 nm, (b) 276 nm and (c) 281 nm grating period at 75 K at different excitation densities.

Optical Materials EXPRESS

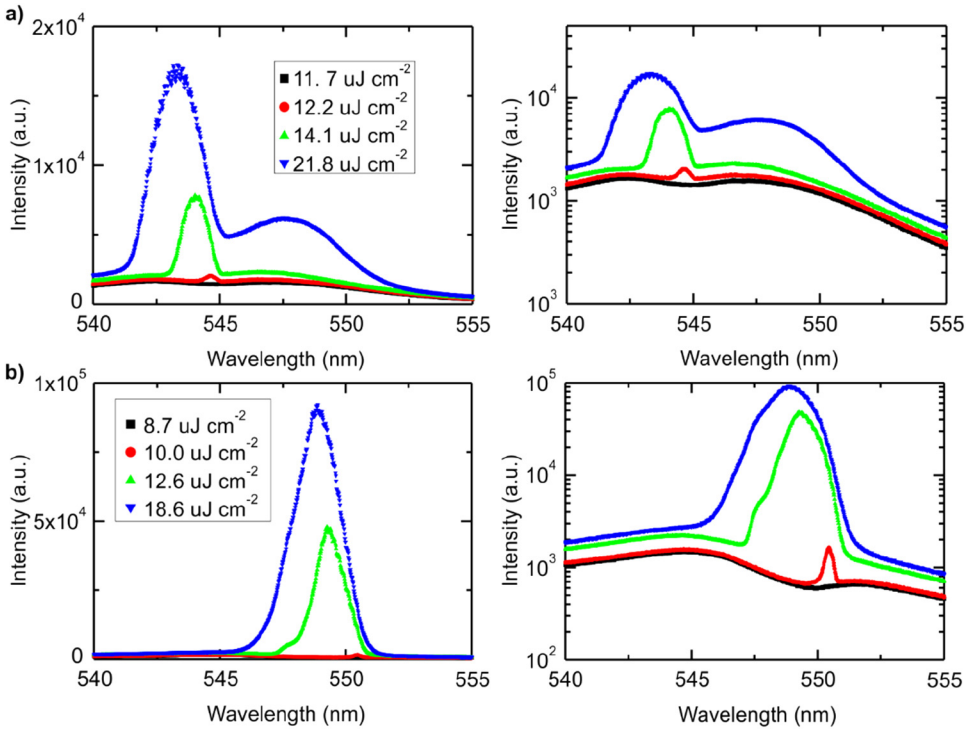

Fig. 10. Linear and logarithmic spectra for (a) 271 nm and (b) 281 nm grating period at 150 K at different excitation densities.

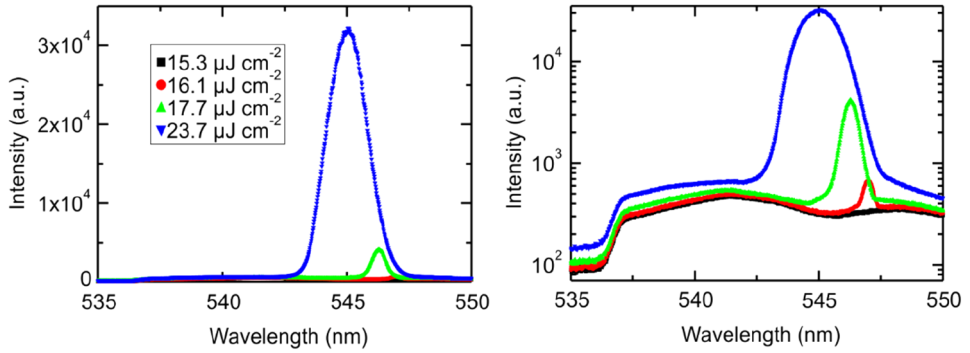

Fig. 11. Linear and logarithmic spectra for 281 nm grating period at 225 K at different excitation densities.

Optical Materials EXPRESS

The structure with the longest wavelength at 5 K has a grating period of 281 nm. It has a higher threshold because it is located at the edge of the photoluminescence. In the logarithmic plot at high energy densities there is also the second peak at 550 nm visible which leads to a broadening of the spectra.

At 75 K all grating resonances are located close to the maximum of the photoluminescence. This means low thresholds and high saturation pump densities for all structures. They all have narrow peaks for low excitation energies above threshold and the broadening can be explained by the second PL peak from ASE which becomes more significant above saturation pump density.

At 150 K one can obtain that in comparison with 75 K the emission peak from the grating with 271 nm is shifted further away from the ASE peak. This leads to a reduction of the efficiency additional to the reduction from the increasing temperature. On the other hand, the emission from the circular grating with 281 nm shifts closer to the ASE peak This leads to an increased emission for high a pump density compared to the emission from the same structure at 75 K while the threshold seems not to be influenced by the position relative to the ASE peak.

At 225 K, stimulated emission can be only observed from the structure with the 281 nm grating period. The exponential increase of the threshold for increasing temperatures as depicted in Fig. 7 has a significantly higher influence than for 75 K.

A.4. Photoluminescence at T = 75 K

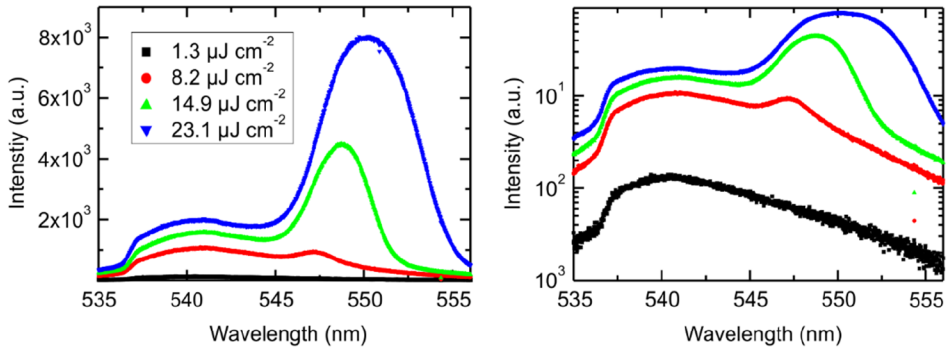

Fig. 12. Linear and logarithmic spectra from the photoluminescence measured from an unstructured part of the fabricated sample at a temperature of 75 K at different excitation densities.

The Photoluminescence was measured by excitation of an unstructured part of the fabricated sample close to the position of the different gratings presented in the measurements above. The photoluminescence increases with increasing pump densities and at a pump density of 8.2 µJ cm^{-2} a second peak starts to emerge. This peak is due to amplified spontaneous emission from the bare perovskite. If the pump density increases furthermore the second peak exhibits a strong red-shift in contrast to the blue-shift for the stimulated emission when increasing the pump density. For increasing temperatures, the threshold for the ASE increases, its peak wavelengths blue-shifts and the photoluminescence in general becomes broader.

Funding

Deutsche Forschungsgemeinschaft (DFG) (FOR730, GI 269/11-1, SPP1391, SPP1839); Bundesministerium für Bildung und Forschung (BMBF) (13N10146, 13N9048, PRINTOPTICS); Carl-Zeiss-Stiftung; H2020 European Research Council (ERC) (COMPLEXPLAS); Baden-Württemberg Stiftung (Spitzenforschung II); Adolphe Merkle Foundation; Universität Stuttgart (open access fund).

Optical Materials EXPRESS

References

1. S. X. Tao, X. Cao, and P. A. Bobbert, "Accurate and efficient band gap predictions of metal halide perovskites using the DFT-1/2 method: GW accuracy with DFT expense," Sci. Rep. **7**(1), 1–9 (2017).
2. S. De Wolf, J. Holovsky, S. J. Moon, P. Löper, B. Niesen, M. Ledinsky, F. J. Haug, J. H. Yum, and C. Ballif, "Organometallic halide perovskites: Sharp optical absorption edge and its relation to photovoltaic performance," J. Phys. Chem. Lett. **5**(6), 1035–1039 (2014).
3. T. Leijtens, S. D. Stranks, G. E. Eperon, R. Lindblad, E. M. J. Johansson, I. J. McPherson, H. Rensmo, J. M. Ball, M. M. Lee, and H. J. Snaith, "Electronic properties of meso-superstructured and planar organometal halide perovskite films: Charge trapping, photodoping, and carrier mobility," ACS Nano **8**(7), 7147–7155 (2014).
4. N. Kitazawa, Y. Watanabe, and Y. Nakamura, "Optical properties of $CH_3NH_3PbX_3$ (X = halogen) and their mixed-halide crystals," J. Mater. Sci. **37**(17), 3585–3587 (2002).
5. J. H. Noh, S. H. Im, J. H. Heo, T. N. Mandal, and S. Il Seok, "Chemical management for colorful, efficient, and stable inorganic-organic hybrid nanostructured solar cells," Nano Lett. **13**(4), 1764–1769 (2013).
6. A. Sadhanala, S. Ahmad, B. Zhao, N. Giesbrecht, P. M. Pearce, F. Deschler, R. L. Z. Hoye, K. C. Gödel, T. Bein, P. Docampo, S. E. Dutton, M. F. L. De Volder, and R. H. Friend, "Blue-Green Color Tunable Solution Processable Organolead Chloride-Bromide Mixed Halide Perovskites for Optoelectronic Applications," Nano Lett. **15**(9), 6095–6101 (2015).
7. T. Miyasaka, A. Kojima, K. Teshima, and Y. Shirai, "Organometal halide perovskites as visible-light sensitizers for photovoltaic cells," J. Am. Chem. Soc. **131**(17), 6050–6051 (2009).
8. NREL, "PV Research Cell Record Efficiency Chart," https://www.nrel.gov/pv/assets/pdfs/pv-efficiency-chart.20190103.pdf. (accessed 07.01.2019)
9. N. Wang, L. Cheng, R. Ge, S. Zhang, Y. Miao, W. Zou, C. Yi, Y. Sun, Y. Cao, R. Yang, Y. Wei, Q. Guo, Y. Ke, M. Yu, Y. Jin, Y. Liu, Q. Ding, D. Di, L. Yang, G. Xing, H. Tian, C. Jin, F. Gao, R. H. Friend, J. Wang, and W. Huang, "Perovskite light-emitting diodes based on solution-processed self-organized multiple quantum wells," Nat. Photonics **10**(11), 699–704 (2016).
10. J. Luo, X. Wang, S. Li, J. Liu, Y. Guo, G. Niu, L. Yao, Y. Fu, L. Gao, Q. Dong, C. Zhao, M. Leng, F. Ma, W. Liang, L. Wang, S. Jin, J. Han, L. Zhang, J. Etheridge, J. Wang, Y. Yan, E. H. Sargent, and J. Tang, "Efficient and stable emission of warm-white light from lead-free halide double perovskites," Nature **563**(7732), 541–545 (2018).
11. J. Xing, Y. Zhao, M. Askerka, L. N. Quan, X. Gong, W. Zhao, J. Zhao, H. Tan, G. Long, L. Gao, Z. Yang, O. Voznyy, J. Tang, Z. H. Lu, Q. Xiong, and E. H. Sargent, "Color-stable highly luminescent sky-blue perovskite light-emitting diodes," Nat. Commun. **9**(1), 1–8 (2018).
12. M. R. Leyden, L. Meng, Y. Jiang, L. K. Ono, L. Qiu, E. J. Juarez-Perez, C. Qin, C. Adachi, and Y. Qi, "Methylammonium Lead Bromide Perovskite Light-Emitting Diodes by Chemical Vapor Deposition," J. Phys. Chem. Lett. **8**(14), 3193–3198 (2017).
13. F. Deschler, M. Price, S. Pathak, L. E. Klintberg, D. D. Jarausch, R. Higler, S. Hüttner, T. Leijtens, S. D. Stranks, H. J. Snaith, M. Atatüre, R. T. Phillips, and R. H. Friend, "High photoluminescence efficiency and optically pumped lasing in solution-processed mixed halide perovskite semiconductors," J. Phys. Chem. Lett. **5**(8), 1421–1426 (2014).
14. H. Zhu, Y. Fu, F. Meng, X. Wu, Z. Gong, Q. Ding, M. V. Gustafsson, M. T. Trinh, S. Jin, and X.-Y. Zhu, "Lead halide perovskite nanowire lasers with low lasing thresholds and high quality factors," Nat. Mater. **14**(6), 636–642 (2015).
15. B. R. Sutherland, S. Hoogland, M. M. Adachi, C. T. O. Wong, and E. H. Sargent, "Conformal organohalide perovskites enable lasing on spherical resonators," ACS Nano **8**(10), 10947–10952 (2014).
16. Q. Zhang, S. T. Ha, X. Liu, T. C. Sum, and Q. Xiong, "Room-Temperature Near-Infrared High - Q Perovskite Whispering- Gallery Planar Nanolasers," Nano Lett. **14**(10), 5995–6001 (2014).
17. M. Saliba, S. M. Wood, J. B. Patel, P. K. Nayak, J. Huang, J. A. Alexander-Webber, B. Wenger, S. D. Stranks, M. T. Hörantner, J. T. W. Wang, R. J. Nicholas, L. M. Herz, M. B. Johnston, S. M. Morris, H. J. Snaith, and M. K. Riede, "Structured Organic-Inorganic Perovskite toward a Distributed Feedback Laser," Adv. Mater. **28**(5), 923–929 (2016).
18. Z. Li, J. Moon, A. Gharajeh, R. Haroldson, R. Hawkins, W. Hu, A. Zakhidov, and Q. Gu, "Room-Temperature Continuous-Wave Operation of Organometal Halide Perovskite Lasers," ACS Nano **12**(11), 10968–10976 (2018).
19. F. Mathies, P. Brenner, G. Hernandez-Sosa, I. A. Howard, U. W. Paetzold, and U. Lemmer, "Inkjet-printed perovskite distributed feedback lasers," Opt. Express **26**(2), A144–A152 (2018).
20. N. Pourdavoud, A. Mayer, M. Buchmüller, K. Brinkmann, T. Häger, T. Hu, R. Heiderhoff, I. Shutsko, P. Görrn, Y. Chen, H. C. Scheer, and T. Riedl, "Distributed Feedback Lasers Based on MAPbBr3," Adv. Mater. Technol. **3**(4), 1700253 (2018).
21. J. R. Harwell, G. L. Whitworth, G. A. Turnbull, and I. D. W. Samuel, "Green Perovskite Distributed Feedback Lasers," Sci. Rep. **7**(1), 11727 (2017).
22. J. Gong, Y. Wang, S. Liu, P. Zeng, X. Yang, R. Liang, Q. Ou, X. Wu, and S. Zhang, "All-inorganic perovskite-based distributed feedback resonator," Opt. Express **25**(24), A1154–A1161 (2017).
23. H. Kim, L. Zhao, J. S. Price, A. J. Grede, K. Roh, A. N. Brigeman, M. Lopez, B. P. Rand, and N. C. Giebink, "Hybrid perovskite light emitting diodes under intense electrical excitation," Nat. Commun. **9**(1), 4893 (2018).
24. D. Sizov, R. Bhat, and C. E. Zah, "Gallium indium nitride-based green lasers," J. Lightwave Technol. **30**(5), 679–699 (2012).
25. M. R. Krames, O. B. Shchekin, R. Mueller-Mach, G. O. Mueller, L. Zhou, G. Harbers, and M. G. Craford, "Status and future of high-power light-emitting diodes for solid-state lighting," J. Disp. Technol. **3**(2), 160–175 (2007).

Optical Materials EXPRESS

26. H. Kogelnik and C. V. Shank, "Stimulated emission in a periodic structure," Appl. Phys. Lett. **18**(4), 152–154 (1971).
27. S. Keyvaninia, S. Verstuyft, L. Van Landschoot, F. Lelarge, G.-H. Duan, S. Messaoudene, J. M. Fedeli, T. De Vries, B. Smalbrugge, E. J. Geluk, J. Bolk, M. Smit, G. Morthier, D. Van Thourhout, and G. Roelkens, "Heterogeneously integrated III-V/silicon distributed feedback lasers," Opt. Lett. **38**(24), 5434 (2013).
28. P. J. Cegielski, S. Neutzner, C. Porschatis, H. Lerch, J. Bolten, S. Suckow, A. R. S. Kandada, B. Chmielak, A. Petrozza, T. Wahlbrink, and A. L. Giesecke, "Integrated perovskite lasers on a silicon nitride waveguide platform by cost-effective high throughput fabrication," Opt. Express **25**(12), 13199 (2017).
29. N. Moll, R. F. Mahrt, C. Bauer, H. Giessen, B. Schnabel, E. B. Kley, and U. Scherf, "Evidence for bandedge lasing in a two-dimensional photonic bandgap polymer laser," Appl. Phys. Lett. **80**(5), 734–736 (2002).
30. C. Bauer, H. Giessen, B. Schnabel, E. B. Kley, C. Schmitt, U. Scherf, and R. F. Mahrt, "A surface-emitting circular grating polymer laser," Adv. Mater. **13**(15), 1161–1164 (2001).
31. X. Sun and A. Yariv, "Surface-emitting circular DFB, disk- and ring- Bragg resonator lasers with chirped gratings: a unified theory and comparative study," Opt. Express **16**(12), 9155 (2008).
32. X. Sun and A. Yariv, "Surface-emitting circular DFB, disk-, and ring-Bragg resonator lasers with chirped gratings. II: nonuniform pumping and far-field patterns," Opt. Express **17**(1), 1–6 (2009).
33. M. S. Alias, I. Dursun, M. I. Saidaminov, E. M. Diallo, P. Mishra, T. K. Ng, O. M. Bakr, and B. S. Ooi, "Optical constants of $CH_3NH_3PbBr_3$ perovskite thin films measured by spectroscopic ellipsometry," Opt. Express **24**(15), 16586 (2016).
34. M. Saliba, K. W. Tan, H. Sai, D. T. Moore, T. Scott, W. Zhang, L. A. Estroff, U. Wiesner, and H. J. Snaith, "Influence of thermal processing protocol upon the crystallization and photovoltaic performance of organic-inorganic lead trihalide perovskites," J. Phys. Chem. C **118**(30), 17171–17177 (2014).
35. S. Gholipour, A. M. Ali, F. Tajabadi, W. Tress, N. Taghavinia, M. Grätzel, A. Abate, F. De Angelis, C. A. Gaggioli, E. Mosconi, A. Hagfeldt, and M. Saliba, "Globularity-Selected Large Molecules for a New Generation of Multication Perovskites," Adv. Mater. **29**(38), 1702005 (2017).
36. G. Niu, X. Guo, and L. Wang, "Review of recent progress in chemical stability of perovskite solar cells," J. Mater. Chem. A **3**(17), 8970–8980 (2015).
37. X. Chen, H. Lu, Y. Yang, and M. C. Beard, "Excitonic Effects in Methylammonium Lead Halide Perovskites," J. Phys. Chem. Lett. **9**(10), 2595–2603 (2018).
38. W. W. Chow and S. W. Koch, *Semiconductor-Laser Fundamentals* (Springer, 1999).
39. H. Linnenbank, M. Saliba, L. Gui, B. Metzger, S. G. Tikhodeev, J. Kadro, G. Nasti, A. Abate, A. Hagfeldt, M. Graetzel, and H. Giessen, "Temperature dependent two-photon photoluminescence of $CH_3NH_3PbBr_3$: structural phase and exciton to free carrier transition," Opt. Mater. Express **8**(3), 511 (2018).
40. S. Yakunin, L. Protesescu, F. Krieg, M. I. Bodnarchuk, G. Nedelcu, M. Humer, G. De Luca, M. Fiebig, W. Heiss, and M. V. Kovalenko, "Low-threshold amplified spontaneous emission and lasing from colloidal nanocrystals of caesium lead halide perovskites," Nat. Commun. **6**(1), 8056 (2015).
41. D. Priante, I. Dursun, M. S. Alias, D. Shi, V. A. Melnikov, T. K. Ng, O. F. Mohammed, O. M. Bakr, and B. S. Ooi, "The recombination mechanisms leading to amplified spontaneous emission at the true-green wavelength in $CH_3NH_3PbBr_3$ perovskites," Appl. Phys. Lett. **106**(8), 081902 (2015).
42. A. M. Soufiani, F. Huang, P. Reece, R. Sheng, A. Ho-Baillie, and M. A. Green, "Polaronic exciton binding energy in iodide and bromide organic-inorganic lead halide perovskites," Appl. Phys. Lett. **107**(23), 231902 (2015).
43. C. Wolf, J. S. Kim, and T. W. Lee, "Structural and Thermal Disorder of Solution-Processed $CH_3NH_3PbBr_3$ Hybrid Perovskite Thin Films," ACS Appl. Mater. Interfaces **9**(12), 10344–10348 (2017).